Int. J. Electrochem. Sci., 11 **(2016)** 6848 – 6861, doi: 10.20964/2016.08.22

International Journal of
ELECTROCHEMICAL
SCIENCE
www.electrochemsci.org

High Photoconversion Efficiency Obtained from Novel TiO_2 Photoanodes

T. A. Aljohani[1,2,*] , *Abdulaziz K. Almutairi*[2]

[1] National Centre for Advanced Materials Technology, King Abdulaziz City for Science and Technology (KACST), Riyadh, 11442 Saudi Arabia.
[2] Excellence Centre for Advanced Materials and Manufacturing, King Abdulaziz City for Science and Technology (KACST), Riyadh, 11442 Saudi Arabia
[*]E-mail: taljohani@kacst.edu.sa

Received: 3 May 2016 / *Accepted:* 29 May 2016 / *Published:* 7 July 2016

High photoconversion efficiency for photoelectrochemical water splitting was obtained using nanocaves TiO_2 and highly uniformed TiO_2 nanotubes. The photoanodes were synthesized via electrochemical anodization of a titanium foil in a glycerol-based solution containing NH_4F at 10 V. Pulse electrodeposition was used to incorporate Cu ions into the uniform TiO_2 nanotubes. The photoconversion efficiency performance was examined under simulated visible light illumination ($\lambda \geq$ 380 nm) in a 1 M solution of NaOH. The photocurrent density, the Mott-Schottky, the EIS, and the photoconversion efficiency measurements were determined. The highest photocurrent density i.e. 5.77 mA cm^{-2} at 1.23 V vs. RHE was obtained from nanocaves TiO_2 photoanode. The incorporation of Cu resulted in a reduction in photocatalytic activity of the oxygen evaluation reaction (OER) and an increase of the hydrogen evolution reaction (HER).

Keywords: Anodization, Titanium dioxide nanotubes, Photoelectrochemical, Photocurrent density, water splitting.

1. INTRODUCTION

Global energy demand is growing dramatically, which underscores the need to find sustainable alternative energy resources. Solar radiation is a rich resource of energy that needs to be harvested, converted, and stored to meet such demand. Photovoltaic (PV) cells, made of semiconductor materials, are widely used for converting solar energy into electricity. However, solar energy still needs further per watt cost reduction and requires additional storage units due to the irregular variations in solar radiation. Meanwhile, photoelectrolysis of water to produce H_2, a clean and renewable energy carrier, via hydrogen evolution reaction (HER) has attracted considerable attention. The production of

hydrogen by water splitting encompasses extraction, conversion, and storage of energy in a single process. Photoelectrolysis of water was first reported in 1972 by Fujishima and Honda[1], who demonstrated that the water splitting can be achieved using a single crystal TiO_2 semiconductor and UV light. TiO_2 is the most preferred material for hydrogen production due to its useful properties such as low cost, nontoxicity, and very high photocorrosion resistance. However, its wide band gap (3 - 3.2 eV) allows the absorption of only UV region of the solar spectrum (i.e., approximately 4%) [2]. Therefore, to improve its sensitivity to the visible sunlight, typically, the band gap of TiO_2 is lowered by metal doping. In 1975, Fujishima and two colleagues[3] investigated the carbon-doped TiO_2 film. They reported an energy conversion efficiency of 0.4% under sunlight. Twenty-sever years later, the energy conversion efficiency was significantly improved to 8.35% by Khan et al.[4], as reported in a highly controversial publication. In 1994, Choi et al.[5] investigated the photoreactivity of TiO_2 doped with 21 different metal ions and noticed that the metal ions could shift its photoresponse into the visible spectrum. Furthermore, Wu et al.[6] developed a qualitative approach to investigate the effects of doped metal ions such as Cr, Mn, Fe, CO, Ni, and Cu on the photocatalytic activity of TiO_2. The fabrication of N-modified TiO_2 nanowire arrays was reported by S. Hoang and coworkers[7] using a simple cobalt treatment, which resulted in shifting the absorption into the visible spectrum.

Recently, a theoretical study predicted that the incorporation of Cu ion into TiO_2 reduces the band gap hence increases photocatalytic activity[8]. This result was only examined with Cu-doped TiO_2 nanoparticles prepared by sol gel method[9][10] [11]. Therefore, it is worthwhile to study Cu ion incorporation into TiO_2 nanotubes, which has not been explored to the best of our knowledge.

Additionally, anodization parameters (e.g. anodization time, voltage, electrolyte type, agitation, temperature) of TiO_2 nanotubes synthesis reported to have a significant effect on energy conversion efficiency. For example, organic based electrolytes produced smoother and longer tubes exhibited higher current efficiency[12][13]. In addition, the agitation found to have an impact on tubes formation rate[14]. Temperature also has a significant consequence on pores size and shapes[15] while varying anodizing potential affects both tubes physical formation and growth rate, which in turn affect the energy conversion efficiency[16][17]. Furthermore, the repetition of the anodization process is used to enhance energy conversion efficiency [18].

Accordingly, this study investigates the effect of solution agitating on the formation of titanium dioxide (TiO_2) nanotubes. In addition, it explores incorporating Cu ions into TiO_2 nanotubes using pulse electrodeposition. Subsequently, their solar energy conversion performance will be determined and discussed.

2. EXPERIMENTAL SECTION

2.1. Synthesis of TiO_2 nanotubes

2.1.1. Surface treatment:

Pure Ti foils (99.6% purity, 0.25-mm thickness, Alfa Aesar) were initially polished with dry sandpaper (3000 grit) followed by 30-micron alumina powder polishing. The polished samples were cleaned in the ultrasonic baths of ethanol and DI water for 5 and 10 min, respectively. As a final step

before the electrochemical anodic oxidation, samples were etched with a HNO_3 [5 M] solution 1:2 for 1 min and then rinsed thoroughly with DI water for 5 min.

2.1.2. Anodic titanium oxidation (ATO):

Titanium dioxide nanotubes (TiO_2 NTs) were prepared by a two-step electrochemical anodization method to obtain well-uniformed nanotubes. Furthermore, it is wildly applied to improve the photocatalytic activity of water splitting [8][20]. The first step was performed at room temperature using a two-electrode configuration cell. Platinum mesh (2.5 cm^2) was used as the counter electrode, and a clean Ti sheet (3 cm^2) was pressed at the O-ring side and connected to the anode. This step was performed using a KEYSIGHT (formerly known as Agilent) N8738A Power Supply (80 V, 42 A, 3360 W) for 15 min, followed by cleaning of the sample with DI water in an ultrasonic bath for 15 min. The exposed electrode area was approximately 0.785 cm^2. The electrolyte solutions were prepared using deionized water with high resistivity (18.2 MΩ-cm), containing NH_4F [0.27 M], glycerol/water (70:30), and $NaSO_4$ [0.5 M].

The second anodization step was performed using a Bio-Logic (SP200) potentiostat in a standard three-electrode configuration, and the current was monitored over time during the experiment that lasted for 24 h to ensure preparing long TiO_2 nanotubes. Platinum mesh and an Ag/AgCl electrode saturated with NaCl were used as the counter and reference electrodes, respectively. Note that magnetic stirrers were applied during the growing of titanium dioxide nanotubes (TiO_2 NTs). The porous TiO_2 photoanodes were prepared using similar procedure. However, in the second anodization step, only natural convention was used.

2.2. Synthesis of Cu/TiO2 nanotubes

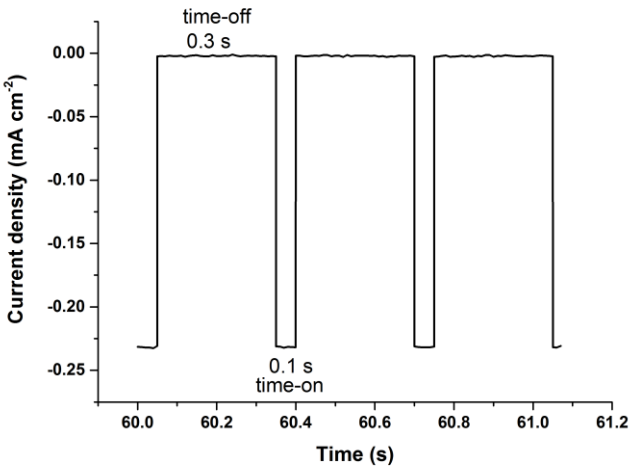

Figure 1. Pulse electrodeposition (PED) parameters for the fabrication of Cu/TiO_2 nanotubes.

A pulse electrodeposition (PED) technique was used to uniformly deposit Cu ions into the TiO_2 NTs. The deposition was carried out in a two-electrode cell containing sodium citrate [0.1 M] and copper sulphate [0.05 M]. The pulse current density of 230 μA cm^{-2} was switched between 0.1 s (ON) and 0.3 s (OFF) intervals during the deposition for 21 min as shown in Fig. 1. The pH of the solution was adjusted to 12 using NaOH.

2.3. Characterization

The morphologies and diameters of the titanium nanotubes were characterized using a field emission scanning electron microscope (FEI SEM, NNL 200, Japan) with an energy dispersive X-ray spectrometer (EDS, Genesis).

The crystallographic structures of pure and Cu-doped TiO_2 nanotubes were investigated using an X-ray diffractometer (D8 Discover, Bruker) with Cu Kα radiation (λ 1.54430 Å, 30 kV, 40 mA)

2.4. Photoelectrochemical measurements

The water splitting efficiency of the TiO_2 nanotubes was evaluated in a 1 M NaOH solution (pH = 13.6) using a commercial photoelectrochemical cell (PECC-2) purchased from Zahner. The photocurrents were obtained using a three-electrode configuration controlled by a Bio-Logic (SP200) potentiostat. A platinum ring and an Ag/AgCl electrode saturated with NaCl were used as the counter and the reference electrodes, respectively. All potentials reported in this study are referred to the reversible hydrogen electrode (RHE). The linear scanning voltammetry (LSV) measurements were recorded at 20 mV s^{-1}. The electrochemical impedance spectra was obtained using a Bio-Logic (SP200) potentiostat/Galvanostat/FRA with an excitation signal of 10 mV amplitude. First, the impedance was scanned as a function of frequency from 200 kHz to 100 MHz at the open circuit potential. Next, the impedance was scanned over a wide potential range at 3 kHz to determine the carrier density and to perform Mott-Schottky analysis.

All of the samples were illuminated by a 300 W Xenon lamp (MAX-303 ASAHI SPECTRA) at a selected wavelength (385- 740 nm) using an embedded filter and a mirror module. The light intensity was calibrated at 100 mW cm^{-2} using a Si photodiode power sensor (THORNLABS, PM200). This was verified before and after experiments to ensure the light stability.

3. RESULTS AND DISCUSSION

3.1. Anodization process

Fig. 2 shows the current density transient curves for two types of TiO_2 photoanodes obtained during the second anodization process in a glycerol/water solution at 10 V. The TiO_2 NTs-A was fabricated in a two-electrode electrochemical cell using a magnetic stirrer, whereas the TiO_2 porous-B was fabricated under natural convection with no magnetic stirrer. Both samples showed a sharp

increase in the initial current density followed by a rapid decrease, which indicates the formation of titanium dioxide. This observed trend was consistent with the earlier reports [9][10][11]. A similar behaviour was shown by the TiO_2 NTs-A and the TiO_2 porous-B at the first three hours of anodization process; however, the TiO_2 NTs-A exhibited a small increase in the current density after 4 hrs. This rise was attributed to the onset of the growth of nanotubes [12][13]. Afterward, the TiO_2 NTs-A showed a quasi-steady state current during rest of the anodization process, which is scribed to equilibrium state between metal electrochemical oxidation i.e. oxide formation reaction (Eq. (1)) and chemical dissolution reaction (Eq. (2))[24].

$$Ti + 2H_2O \rightarrow TiO_2 + 4H^+ + 4e^- \quad (1)$$

$$TiO_2 + 6F^- + 4H^+ \rightarrow [TiF_6]^{2-} \quad (2)$$

However, the TiO_2 porous-B showed a higher current with periodical oscillations after 6 hrs. This periodical current oscillation was also observed by Macak et al.[20] and attributed to the structure of ripples formation at the sidewalls of the tubes at acidic-fluoride-based electrolyte.

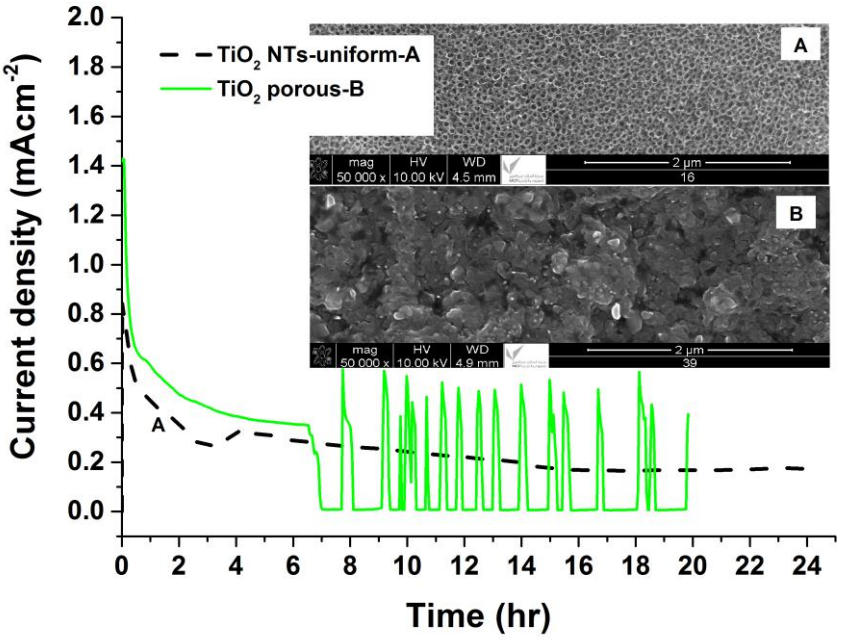

Figure 2. Current density versus anodizing time curve for TiO_2 nanotubes grown in a glycerol/water-based electrolyte solution (70:30) containing 0.27 M NH_4F at room temperature. The inset shows the SEM images after the anodization process (A) with agitation and (B) without agitation.

Because of the current oscillation, the dynamic equilibrium between the above reactions was not more likely to occur for the TiO_2 porous-B. Therefore, different morphologies were obtained (see the inset Fig. 2). We assume that the agitation of the solution balances the fluoride [F^-] ions diffusion to the metal surface, and the effusion of the $[TiF_6]^{2-}$ complex from the surface; thus a uniform TiO_2 nanotubes was obtained when agitation applied. This notion is agreed with a recent report [11]. On the other hand, when no agitation was used, the balance between these two reactions was disturbed during

the formation of the TiO_2 porous-B. Therefore, the TiO_2 porous-B showed a nano-caves TiO_2 surface as seen in Fig. 2B. A comparable result has been reported elsewhere [14]. Probably, the high viscosity of the electrolyte made agitation important; thus, this may not be the case when acidic electrolyte is used. Another interpretation[15] has attributed the appearance of irregular morphology to the variations in the etch rate of different crystal planes.

3.2. Morphology analysis

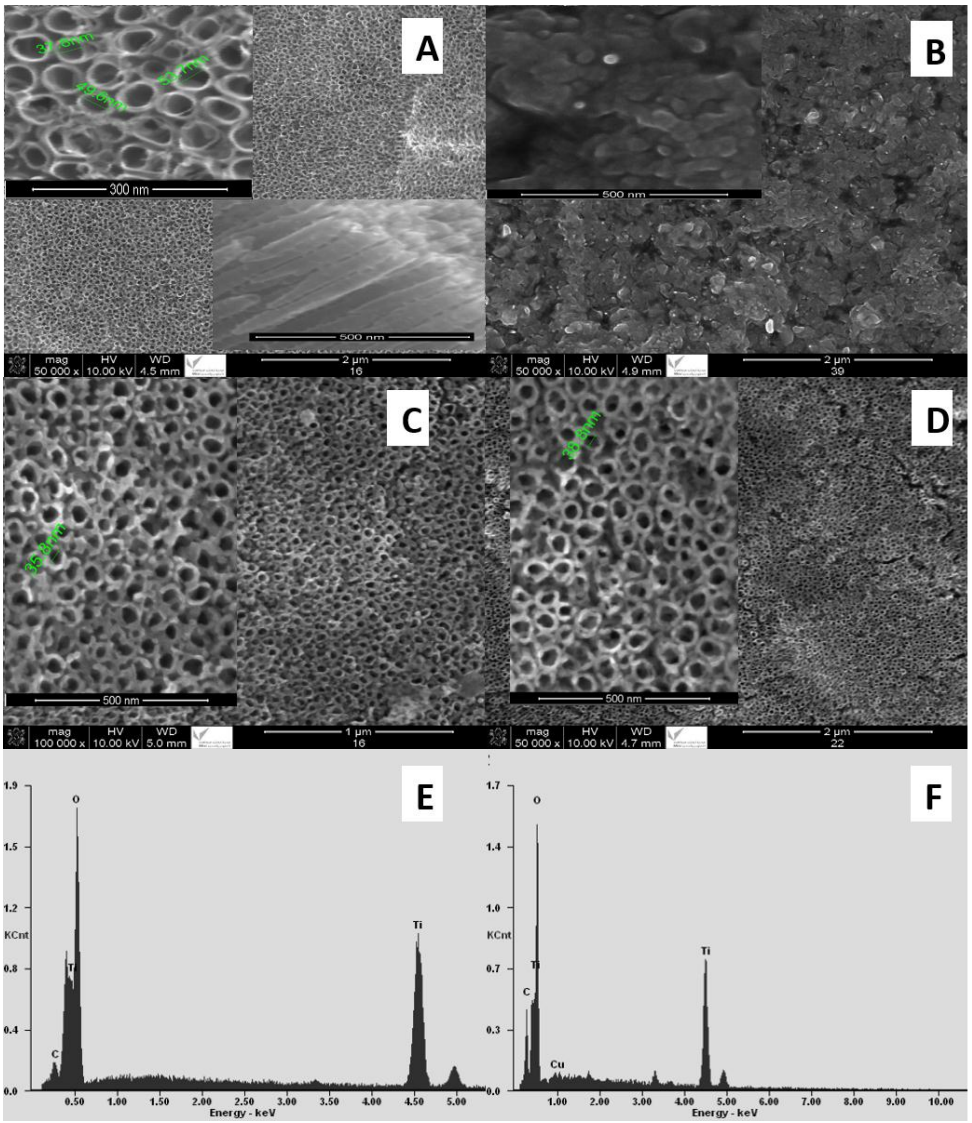

Figure 3. FE-SEM images of pure and Cu-doped TiO_2 nanotubes synthesised in a solution containing glycerol/water (70:30), 0.27 M NH_4F, and 0.5 M Na_2SO_4 at 10 V: (A) Annealed-uniform TiO_2 nanotubes (with agitation during the anodization process), (B) Annealed-porous TiO_2 (without agitation during the anodization process), (C) Annealed Cu-doped TiO_2 nanotubes, (D) As-deposited Cu-doped TiO_2 nanotubes, (E) EDX analysis of the annealed TiO_2 nanotubes shown in (A), and (F) EDX analysis of the annealed Cu-doped TiO_2 nanotubes shown in (C). The insets show cross section and zoomed in images.

Fig. 3 shows the FE-SEM images and EDS results of pure TiO_2 and Cu-doped TiO_2 NTs. Fig. 3 (A) and (B) display pure TiO_2 NTs and porous TiO_2 fabricated with and without agitation, respectively, using a solution containing glycerol/water (70:30), 0.27 M NH_4F, and 0.5 M Na_2SO_4 at 10 V. Agitation during the anodization process resulted in uniform TiO_2 NTs, as shown in Fig. 3A. However, the porous TiO_2 shows nano-caves morphology (see Fig. 3B). In addition, no tubes are observed. This is ascribed to the chemical imbalance between the titanium dioxide formation and chemical dissolution reactions, which is strongly affected by the agitation particularly in high viscous electrolyte, as discussed in details in the former section. The average diameter of TiO_2 NTs (Fig. 3A) is found to be 47 nm that is reduced to approximately 39 nm after the pulse electrodeposition of Cu (Fig. 3C, 3D). The EDS results before and after Cu doping (as shown in Fig. 3 (E) and (F)) confirmed the presence of Cu. However, we should emphasize that the EDS analysis is not enough but it was the available tool during samples preparation. Furthermore, the nanotubes length is 1µm tubes obtained by long anodization time, which was lasted for 24 hours (see the inset Fig. 3A). The tubes length, size and geometrical shape considerably affect solar energy conversion efficiency[26][19].

3.3. XRD analysis

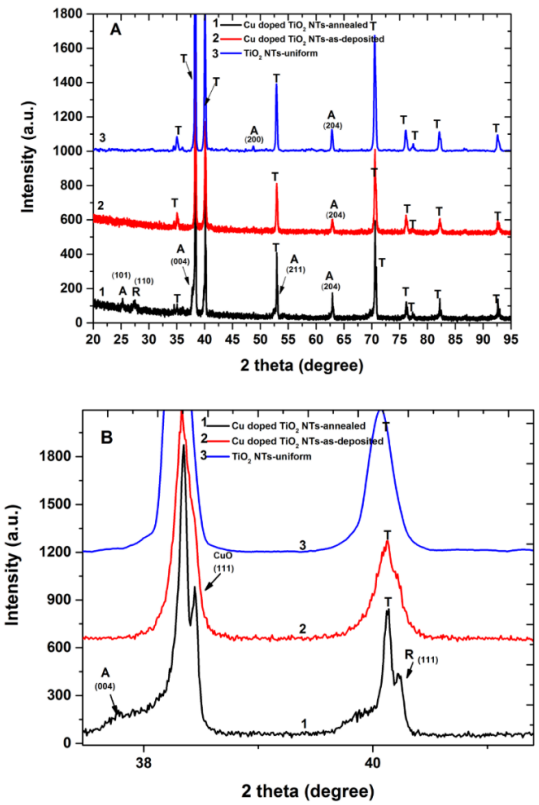

Figure 4. (A) XRD patterns of pure and Cu-doped TiO_2 nanotubes. The samples were annealed at 600 °C in air for 4 h at a heating rate of 50 °C/min. The XRD patterns showed peaks corresponding to pure titanium (T), anatase (A), and rutile (R) phases, (B) Selected peaks of pure and Cu-doped TiO_2 nanotubes are the additional peaks corresponding to the rutile phase and the CuO (002) plane. For the black and white print samples were labeled as 1, 2, 3.

The X-ray diffraction patterns of pure and Cu-doped TiO_2 nanotubes are shown in Figure 4. The annealed TiO_2 nanotubes showed anatase TiO_2 as the dominant phase (Fig. 4A-blue). A similar XRD pattern was obtained for Cu-doped TiO_2 nanotubes (Fig. 4A- red) although a peak corresponding to anatase (200) at ca 49° has disappeared. After annealing at 600 °C in air (Fig. 4B-black), Cu-doped TiO_2 nanotubes display new peaks at 37.9° and 53° corresponding to the (004) and (211) planes, and at 27. 5° and 40.25° corresponding to the (110) and (111) planes, which are indexed to the anatase and rutile phases, respectively, as reported elsewhere[17]–[19]. The latter anatase and rutile peaks, obtained after the annealing of the Cu-doped TiO_2 nanotube, is attributed to the second annealing. In addition, another peak related to the CuO (002) plane is observed at 38.45°[30](see Figure 4B-black). This peak appeared only in the annealed Cu-doped TiO_2 nanotubes.

3.5. Photoelectrochemical results

The water splitting efficiency of TiO_2 photoanodes was investigated in a 1 M NaOH solution (pH = 13.6). Figure 5 shows the photocurrent density versus applied potential curves for pristine nanocave-porous, nanotubes, and Cu-doped TiO_2 nanotubes. The dark currents were very small and did not show any increase until 1.8 V vs. RHE. The best photocurrent density was found to be 5.75 mA cm^{-2} at 1.23 V vs. RHE and was obtained from the highly porous undoped annealed TiO_2. The uniform TiO_2 nanotubes exhibited the second best photocurrent density of 4.75 mA cm^{-2} at 1.23 V vs. RHE. We assume that the novel nanocave-porous annealed TiO_2, yet has not approved, contains less recombination centres compared to the uniform TiO_2 nanotubes.

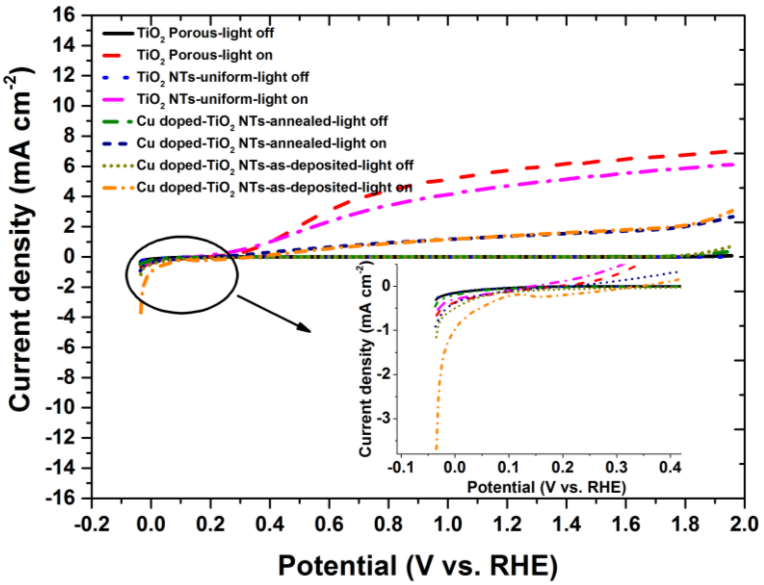

Figure 5. Linear voltammetry scan of the undoped and Cu-doped TiO_2 nanotubes in a 1 M solution of NaOH. Samples were illuminated by visible light (≥ 385 nm) at 100 mW cm^{-2}.

The annealed and as-deposited Cu-doped TiO_2 nanotubes showed similar photocurrent density, which was approximately four times lower than that of the undoped nanocave-porous and uniform

TiO_2 nanotubes. However, the hydrogen evolution reaction remarkably increased after Cu doping (see the inset in Fig. 5). This coincides with the formation of the CuO (002) phase observed after Cu doping as shown in Fig. 4B. The copper oxide was frequently used as p-type photocathode [8], [11], [30]–[37], illustrating the increase of the hydrogen evolution reaction. The negative offset potentials of the annealed and as-deposited Cu doped TiO_2 nanotubes were 0.35 and 0.24 V, respectively. These values are much higher than the 0.17 and 0.14 V negative offset potentials of the undoped nanocave-porous and uniform TiO2 nanotubes. This result indicates that Cu doping increased the concentration of oxygen vacancies, thereby shifting the offset potential towards more negative value[21].

Electrochemical impedance measurements (Fig. 6) shows a small charge transfer resistance under illumination (inset figure), and indicates an increase in charge mobility in the space charge region. Moreover, the dopant ions increased the charge mobility in Cu-doped TiO_2 nanotubes because of their smaller charge resistance. Nevertheless, the photocurrent density of the Cu-doped TiO_2 nanotubes was lower than that of the undoped TiO_2 nanotubes as shown in Fig. 5. The reason of such a reduction is still ambiguous. However, we suspect this is either due to fast recombination rate of the generated electron-hole pairs; therefore, fewer holes become available for the oxidation evolution reaction at the electrode/electrolyte interface. This conclusion is consistent with the results reported by Radecka et al. [22], in which the authors found that the recombination rate became three times faster, and the photocurrent density was reduced after doping the TiO_2 nanotubes with Cr. Alternatively, the incorporation of copper may resulted in a competition between oxidation and hydrogen evolution reactions. The latter analysis is supported by the increment of the hydrogen evolution observed in the photocurrent measurements (see the inset in Fig. 5). Another finding here is that copper doping improves the charge mobility significantly as presented in Fig. 6. Consequently, our next aim is to study the photocurrent response while using a hole scavenger. This probably will enlighten charge transport at electrode/electrolyte interface.

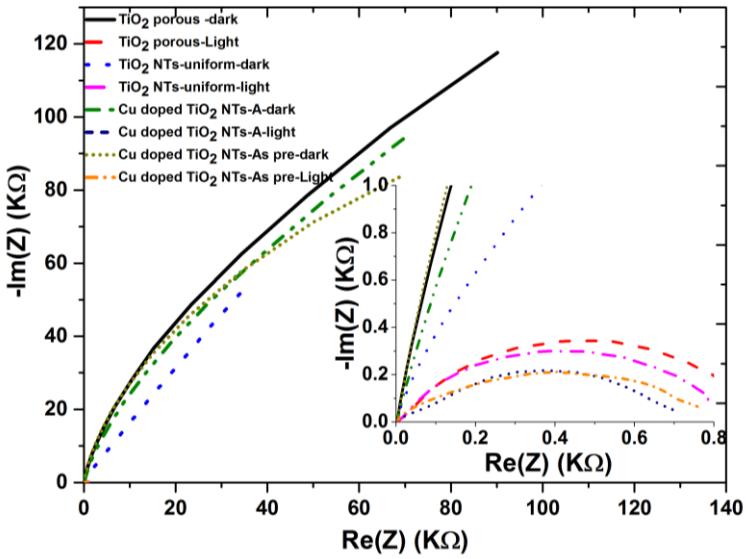

Figure 6. Electrochemical impedance spectra of pristine and Cu-doped TiO_2 porous/nanotubes with and without illumination in a 1 M solution of NaOH at the open circuit potential.

Additionally, the capacitance at the electrode/ electrolyte interface was measured as a function of the applied potentials at 3 kHz without illumination. The Mott-Schottky plots are presented in Fig. 7. The doped and undoped TiO_2 nanotubes exhibited positive slopes, indicating n-type semiconductor behaviour. The carrier density (N_d) and the flatband potential (E_{FB}) were calculated using the slope of the linear region and the y intercept (E_{app} = 0 V), respectively, according to the Mott-Schottky equation (1),

$$\frac{1}{C^2} = \frac{2}{N_D e \varepsilon_o \varepsilon}\left[(U_S - U_{FB}) - \frac{K_B T}{e}\right] \qquad (1)$$

where C is the space charge capacitance of the semiconductor, N_D is the electron carrier density, e is the elemental charge value, ε_o is the permittivity of vacuum, ε is the relative permittivity of the semiconductor, U_S is the applied potential, K_B is the Boltzmann constant, and T is the temperature.

Cu-doped TiO_2 nanotubes shows an enhancement in the carrier density and a greater slope compared with that of the undoped TiO_2 nanotubes as seen in Fig. 7. This behaviour is attributed to the increase in oxygen vacancies concentration because of Cu^{2+} ions with a lower valance replacing Ti^{4+} ions [19], [23]. Therefore, Cu-doped TiO_2 nanotubes exhibited a higher carrier density. The undoped porous TiO_2 showed slightly more carrier density than that of the undoped uniform TiO_2 nanotubes (Fig. 7). A similar observation has been reported previously[24]. The flatband potentials extrapolated from the capacitance measurements, i.e., the Mott-Schottky plots were more negative than the ones obtained from the linear voltammetry scan presented in Table 1. However, the difference was within the acceptable range (~ 0.2 V)[25], [26], with the exception of ~ 0.4 V for the as-deposited Cu doped TiO_2 nanotubes. The observed behaviour of $1/C^2$ vs. V is not always linear due to several factors; including the surface state, the back contact capacitance, and the resistance of Helmholtz layer, which are typically neglected in the capacitance measurement [27]. Therefore, the flatband potentials extrapolated from the photocurrent response (Fig. 5) are more reliable.

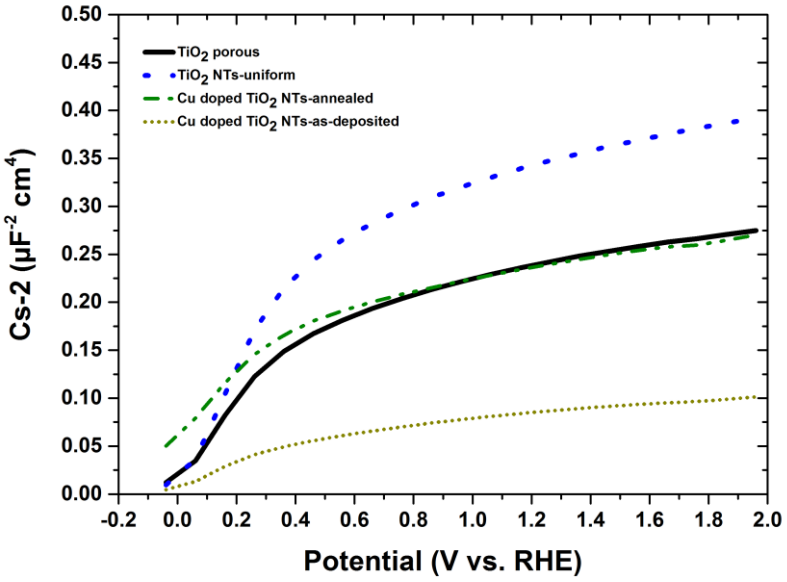

Figure 7. Mott-Schottky plots for Cu-doped and the undoped TiO_2 porous/uniform nanotubes in a 1 M solution of NaOH. The measurements were obtained at 3 kHz.

The energy conversion efficiency (ECE) η_c was calculated using equation 2, and the results are presented in Fig. 8,

$$\eta_c(\%) = J_p\left[\frac{(E^{\circ}_{rev} - |E_{app}|)}{I_{light}}\right] \times 100 \qquad (2)$$

where η_c is the energy conversion efficiency, J_P is the photocurrent density, E^{o}_{rev} is the standard reversible potential of 1.23 V vs. RHE, E_{app} is the applied potential = E_{meas} - E_{ocp}, where E_{meas} is the potential (vs. Ag/AgCl) of the working electrode, E_{ocp} is the working electrode potential (vs. Ag/AgCl) under open circuit condition, and I_{light} is the incident light intensity (100 mW cm^{-2}).

The maximum value of η_c was found to be 2.7% at 0.75 V vs. RHE (-0.211 V vs. Ag/AgCl) and was obtained from the undoped porous TiO_2. The uniform TiO_2 nanotubes showed lowered efficiency. The porous TiO_2 is believed to have higher surface area and less recombination centre as discussed earlier hence showed better efficiency. Yet, This efficiency (η_c) was significantly higher compared with the values reported in the literature [2], [28]–[30]. In addition, the energy conversion efficiency η_c decreased remarkably after Cu doping. This agrees with the photocurrent response observed in Fig. 5. Therefore, conclusion can be drawn here that Cu incorporating into TiO_2 nanotubes is reduced the photocatalytic activity of the oxygen evolution reaction whether it accelerates recombination rate of generated electron-hole pairs or activates the hydrogen evolution reaction. All the previous results are summarized in Table 1.

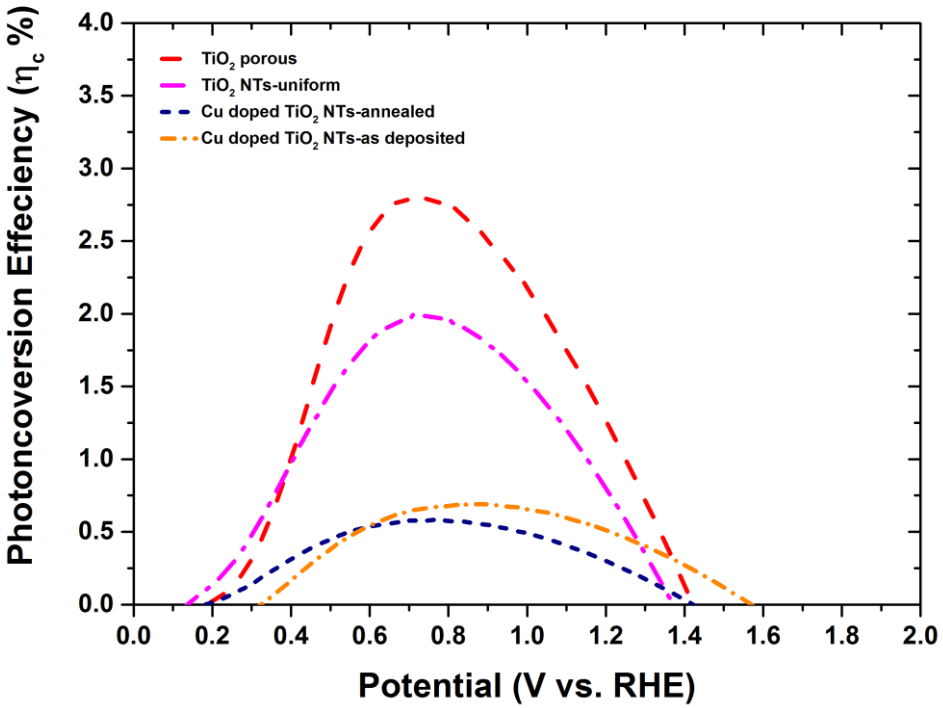

Figure 8. The plot of energy conversion efficiency (ECE) η_c versus applied potential. The applied potential was calculated according to the equation, $E_{app} = E_{meas} - E_{ocp}$.

Table 1. Summary of the results extrapolated from the photocurrent density and the Mott-Schottky plots.

Samples types	Photocurrent density (mA cm^{-2}) at 1.23 V vs. RHE	Flatband potential*(mV) vs. RHE	Carrier density (cm^{-3})	Photoconversion efficiency (%) at 1.23 V vs. RHE
TiO_2 NTs-Porous	5.75	-0.047^a , 0.191^b	12.41 X 10^{18}	1.12
TiO_2 NTs-uniform	4.75	-0.060^a , 0.131^b	9.83 X 10^{18}	0.63
Cu doped TiO_2 NTs-Annealed	1.37	-0.217^a, 0.191^b	16.85 X 10^{18}	0.63
Cu doped TiO_2 NTs-as deposited	1.37	-0.063^a , 0.341^b	38.81 X 10^{18}	0.40

[a] Flatband potential from Mott-Schottky plot.
[b] Flatband potential from Linear voltammetry scan (LVS).

4. CONCLUSION

In conclusion, we synthesized novel porous and uniform TiO_2 nanotubes with different morphologies. The uniform TiO_2 nanotubes were doped with copper using a pulse electrodeposition. The undoped TiO_2 porous/nanotubes demonstrated the highest photocurrent density and energy conversion efficiency (η_c). The carrier density increased noticeably after Cu doping. To sum up, the incorporation of copper reduced the photocatalytic activity of the oxygen evolution reaction and increased the photocatalytic activity of the hydrogen evolution reaction.

ACKNOWLEDGEMENT
Authors would like to acknowledge King Abdulaziz City for Science and Technology (KACST) for funding this work (36-1221).

References

1. A. Fujishima and K. Honda, *Nature*, 238 (1972) 37-38.
2. Z. Zhang, L. Zhang, M. N. Hedhili, H. Zhang, and P. Wang, *Nano Lett.*, 13 (2013) 14-20.
3. A. Fujishima, K. Kohayakawa, and K. Honda, *J. Electrochem. Scociety*, 122 (1975) 1487–1489.
4. S. U. M. Khan, *Science (80-.).*, *Nano Lett.*, 297 (2002) 2243–2245.
5. W. Choi, A. Termin, and M. R. Hoffmann, *J. Phys. Chem.*, 98 (1994) 13669–13679.
6. S. X. Wu, Z. Ma, Y. N. Qin, X. Z. Qi, and Z. C. Liang, *Acta Phys. - Chim. Sin.*, 20 (2004) 138–143.
7. S. Hoang, S. Guo, N. T. Hahn, A. J. Bard, and C. B. Mullins, *Nano Lett.*, 12 (2012) 26–32.

8. B. Ao, Z. Zhang, T. Tang, and Y. Zhao, *Solid State Commun.*, 204 (2015) 23–27.
9. Z. Xi, C. Li, L. Zhang, M. Xing, and J. Zhang, *Int. J. Hydrogen Energy*, 39 (2014) 6345–6353.
10. N. Roy, Y. Sohn, K. T. Leung, and D. Pradhan, *J. Phys. Chem.*, 118 (2014) 29499-29506.
11. R. Bashiri, N. M. Mohamed, C. F. Kait, and S. Sufian, *Int. J. Hydrogen Energy*, 40 (2015) 6021–6037.
12. J. M. Macak and P. Schmuki, *Electrochim. Acta*, 52 (2006) 1258–1264.
13. J. M. Macak, H. Tsuchiya, L. Taveira, S. Aldabergerova, and P. Schmuki, *Angew. Chem. Int. Ed. Engl.*, 44 (2005) 7463–7465.
14. S. Mohapatra, M. Misra, V. Mahajan, and K. Raja, *J. Catal.*, 246 (2007) 362–369.
15. G. D. Sulka, J. Kapusta-Kołodziej, A. Brzózka, and M. Jaskuła, *Electrochim. Acta*, 104 (2013) 526–535.
16. J. M. Macak, H. Tsuchiya, a. Ghicov, K. Yasuda, R. Hahn, S. Bauer, and P. Schmuki, *Curr. Opin. Solid State Mater. Sci.*, 11 (2007) 3–18.
17. Y. Sun and K.-P. Yan, *Int. J. Hydrogen Energy*, 39 (2014) 11368–11375.
18. Z. Zhang, M. F. Hossain, and T. Takahashi, *Int. J. Hydrogen Energy*, 35 (2010) 8528–8535.
19. Z. Zhang and P. Wang, *Energy Environ. Sci.*, 5 (2012) 6506-6512.
20. J. Gong, Y. Lai, and C. Lin, *Electrochim. Acta*, 55 (2010) 4776–4782.
21. H. E. Prakasam, K. Shankar, M. Paulose, O. K. Varghese, and C. A. Grimes, *J. Phys. Chem.*, (2007) 7235–7241.
22. J. M. Macak, H. Hildebrand, U. Marten-Jahns, and P. Schmuki, *J. Electroanal. Chem.*, 621 (2008) 254–266.
23. G. K. Mor, O. K. Varghese, M. Paulose, K. Shankar, and C. a. Grimes, *Sol. Energy Mater. Sol. Cells*, 90 (2006) 2011–2075.
24. H. Nanjo, F. M. B. Hassan, S. Venkatachalam, N. Teshima, K. Kawasaki, T. Aizawa, T. Aida, and T. Ebina, *J. Power Sources*, 195 (2010) 5902–5908.
25. S. Farsinezhad, A. N. Dalrymple, and K. Shankar, *Phys. Status Solidi*, 211 (2014) 1113–1121.
26. K. Shankar, G. K. Mor, H. E. Prakasam, S. Yoriya, M. Paulose, O. K. Varghese, and C. a Grimes, *Nanotechnology*, 18 (2007) 065707.
27. J. Yan, G. Wu, N. Guan, L. Li, Z. Li, and X. Cao, *Phys. Chem. Chem. Phys.*, 15 (2013) 10978–10988.
28. E. K. Ylhäinen, M. R. Nunes, a. J. Silvestre, and O. C. Monteiro, *J. Mater. Sci.*, 47 (2012) 4305–4312.
29. X. Yang, S. Wang, H. Sun, X. Wang, and J. Lian, *Trans. Nonferrous Met. Soc. China*, 25 (2015) 504–509.
30. G. K. Mor, O. K. Varghese, R. H. T. Wilke, S. Sharma, K. Shankar, T. J. Latempa, K. Choi, and C. A. Grimes, *Nano Lett.*, 8 (2008) 1906–1911.
31. C. Li, Y. Li, and J. Delaunay, *ACS Appl. Mater. Interfaces*, 6 (2014) 480–486.
32. G. Magesh, E. Sun, H. Joon, M. Banu, J. Yul, and J. Hyun, *J. Mater. Chem.*, 2 (2014) 2044–2049.
33. R. Liu, E. A. Kulp, F. Oba, E. W. Bohannan, F. Ernst, J. A. Switzer, R. V September, V. Re, M. Recei, and V. December, *Chem. Mater.*, 17 (2005) 725–729.
34. Y. Yang, J. Han, X. Ning, J. Su, J. Shi, W. Cao, and W. Xu, *Int. J. Energy Res.*, 40 (2016) 112-123.
35. M. Hara, T. Kondo, M. Komoda, S. Ikeda, K. Shinohara, and A. Tanaka, *Chem. Commun.*, 2 (1998) 357–358.
36. L. C. Liau, Y. Lin, and Y. Peng, *J. Phys. Chem.*, 117 (2013) 26426–26431.
37. Y.-K. Hsu, C.-H. Yu, Y.-C. Chen, and Y.-G. Lin, *J. Power Sources*, 242(2013) 541–547.
38. G. Wang, H. Wang, Y. Ling, Y. Tang, X. Yang, R. C. Fitzmorris, C. Wang, J. Z. Zhang, and Y. Li, *Nano Lett.*, 11 (2011) 3026–3033.
39. M. Radecka, M. Rekas, a. Trenczek-Zajac, and K. Zakrzewska, *J. Power Sources*, 181(2008) 46–55.

40. K. S. Raja, V. K. Mahajan, and M. Misra, *J. Power Sources*, 159 (2006) 1258–1265.
41. S. Palmas, a. M. Polcaro, J. R. Ruiz, a. Da Pozzo, M. Mascia, and a. Vacca, *Int. J. Hydrogen Energy*, 35 (2010) 6561–6570.
42. B. Y. H. R. Sprunken, R. Schumacher, N. Schindler, and W. Germany, *Faraday Discuss. Chem. Soc.*, 70 (1980) 55-66.
43. M. a. Butler, *J. Appl. Phys.*, 48 (1977) 1914-1920.
44. R. Beranek, *Adv. Phys. Chem.*, 2011 (2012) 1–20.
45. C. Sci, M. Liu, D. L. Snapp, and H. Park, *Chem. Sci.*, (2011) 80–87.
46. H. A. Hamedani, N. K. Allam, H. Garmestani, and M. A. El-sayed, *J. Phys. Chem.*, (2011) 13480–13486.